Taylor & Francis
Taylor & Francis Group

Angular distribution models anisotropic correction factors and sun glint: a sensitivity study

CÉDRIC BERTRAND*, NICOLAS CLERBAUX, ALESSANDRO IPE, STEVEN DEWITTE and LUIS GONZALEZ

Royal Meteorological Institute of Belgium, Department of Observations, Section Remote Sensing from Space, Avenue Circulaire 3, B-1180 Brussels, Belgium

Because radiometers do not measure the Earth's outgoing fluxes directly, angular distribution models (ADMs) are used to invert measured radiances at the top of atmosphere (TOA) to fluxes. In this study, we have investigated if the use of the newly developed clear ocean Clouds and the Earth's Radiant Energy System (CERES) broadband short wave (SW) ADMs from the Tropical Rainfall Measuring Mission (TRMM) satellite will allow reliable estimation of the instantaneous reflected SW fluxes at the TOA when the measured radiances are contaminated by sun glint. Using SW fluxes estimations computed from Meteosat-7 visible radiances as a surrogate of the forthcoming Geostationary Earth Radiation Budget SW fluxes, our results indicate that while CERES-TRMM ADMs angular resolution presents an advance over the previously built Earth Radiation Budget Experiment (ERBE) ADMs, the angular resolution is still too coarse to suitably define anisotropic correction factors in the sunlight region. SW fluxes are overestimated in the strong sun glint region and underestimated in the surrounding regions. Nevertheless, we show that by combining the high temporal sampling of the sun glint regions afforded by the geostationary orbit of the instrument with information contained in the clear ocean wind-speed-dependent CERES-TRMM ADMs, an improved estimation of the reflected SW flux at the TOA is possible by comparison to a simple ADM flux interpolation.

1. Introduction

The determination of the Earth's Radiation Budget (ERB), which represents the balance between incoming energy from the Sun and outgoing thermal (long wave) and reflected (short wave) energy from the Earth, is essential to atmospheric modelling and climate studies. Satellite ERB data are fundamental to the development of realistic climate models and studying natural and anthropogenic perturbations of the climate (Ramanathan 1987). However, space-borne radio-meters cannot measure the Earth outgoing short wave (SW) and long wave (LW) fluxes directly. Rather, they can only measure the radiance instantaneously in a

*Corresponding author. Email: cedric.bertrand@oma.be

single viewing direction. Flux, F, is related to radiance, L, as follows:

$$F(\theta_s) = \int\limits_0^{2\pi} \int\limits_0^{\pi/2} L(\theta_s, \theta_v, \phi)\cos\theta_v \sin\theta_v \, d\theta_v \, d\phi$$

where θ_s is the solar zenith angle, θ_v, the observer viewing zenith angle, and ϕ the relative azimuth angle defining the azimuth angle position of the observer relative to the solar plane (see figure 1). Analysis of satellite measurements for ERB determination requires information about the angular characteristics of radiation that is reflected (SW) and emitted (LW) from the Earth–atmosphere system (Smith *et al.* 1986). These angular characteristics can be defined by models which express, for an imaginary surface element at the top of the atmosphere (TOA), the outgoing radiance intensity as a function of the total hemispheric flux leaving the element (Suttles *et al.* 1988). Angular distribution models (ADMs) are used to relate the measured radiances to fluxes at the given solar angle, satellite-viewing geometries, surface, and atmospheric conditions:

$$F_{ani}(\theta_s) = \frac{\pi L(\theta_s, \theta_v, \phi)}{R(\theta_s, \theta_v, \phi)} \tag{1}$$

where R, the ADM dependent anisotropic factor for a given scene type and viewing geometry, is the ratio between the assumed Lambertian flux to the real flux (Suttles *et al.* 1988). As an example, if the reflected (or emitted) energy is spatially uniform, the anisotropic factor will be 1 in all observation directions, and the flux can be computed from the measured radiance by simply multiplying by a factor of π.

Basically, SW ADMs are constituted by anisotropic factors, R, and (broadband) albedos, A. Each ADM is constructed from a large ensemble of radiance measurements that are sorted into discrete angular bins and parameters that define the ADM scene type (e.g. ocean, land, snow, and clouds). The ADM anisotropic
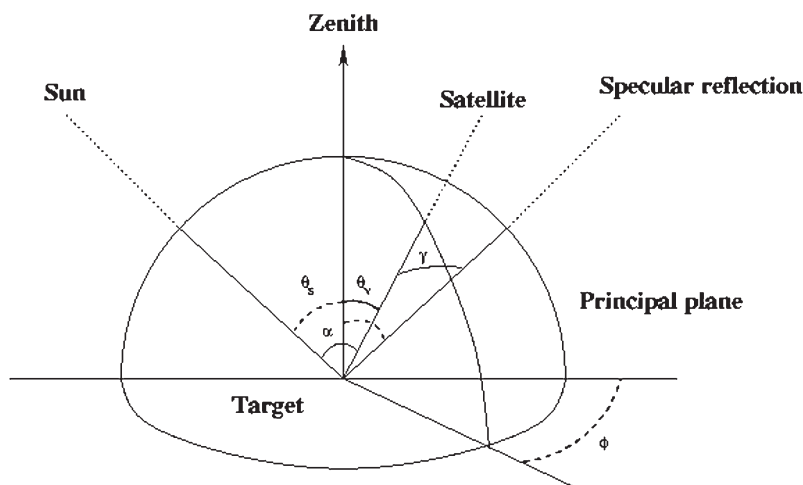

Figure 1.   Sun glint geometry.

factors for a given scene type j are given by (Loeb *et al.* 2002):

$$R_j(\theta_{si}, \theta_{vk}, \phi_l) = \frac{\pi L_j(\theta_{si}, \theta_{vk}, \phi_l)}{F_j(\theta_{si})}$$

where $L_j(\theta_{si}, \theta_{vk}, \phi_l)$ is the mean outgoing broadband radiance at TOA (corrected for the Earth–Sun distance) for a given interval of solar zenith angle θ_{si}, viewing zenith angle θ_{vk}, and relative azimuth angle ϕ_l; $F_j(\theta_{si})$ is the corresponding flux determined by integration of $L_j(\theta_{si}, \theta_{vk}, \phi_l)$ over all upwelling directions. The broadband albedos for a given scene type j are given by:

$$A_j(\theta_{si}) = \frac{F_j(\theta_{si})}{E_o \cos \theta_{si}}$$

where E_o is the solar constant corrected for the Sun–Earth distance.

In principle, when the angular distribution of the energy is known (or can be characterized by the use of an ADM), equation (1) can be used to estimate TOA flux in any viewing geometry. However, when the satellite viewing geometry tends towards the ocean specular reflection direction, the radiance increase for a change in angle as small as $1°$ can be quite large. Because such changes are in practice unresolved by the relatively coarse angular bins resolution used to define ADMs, instantaneous TOA flux estimates are generally unreliable for footprints near the specular reflection direction (see figure 1). Consequently, the radiance-to-flux conversion is generally not performed in the sun glint regions. However, ignoring these samples (e.g. by not providing a TOA flux estimate) can introduce biases in regional mean fluxes because fluxes over cloudy portions of a region will contribute disproportionately to the overall regional mean. To avoid this, Loeb *et al.* (2003) propose bypassing radiance measurements affected by sun glint and estimate fluxes in cloud-free sun glint by the clear ocean wind-speed-dependent ADM TOA flux (actually the albedo) interpolated at the solar zenith angle of the observation:

$$F_{alb}(\theta_s) = E_o \cos \theta_s A(\theta_s) \tag{2}$$

In the present paper, we have investigated if the newly developed Clouds and the Earth's Radiant Energy System (CERES) (Wielicki *et al.* 1996) broadband SW ADMs (Loeb *et al.* 2003) from the Tropical Rainfall Measuring Mission (TRMM) satellite (Kummerow *et al.* 1998) are suitable when performing radiance-to-flux conversion from clear ocean radiance measurements contaminated by sun glint. Moreover, being involved in the Geostationary Earth Radiation Budget (GERB) radiometer (Harries and Crommelynck 1999) ground segment, we have also investigated if it is possible to improve Loeb *et al.*'s climatological ADM flux estimate approach (equation (2)) in regard to the high temporal sampling afforded by geostationary data. The GERB ground segment aims to deliver nearly real-time estimates of the radiation budget for the regions covered by Meteosat Second Generation (MSG-1) (Schmetz *et al.* 2002) at the 3×3 Spinning Enhanced Visible and Infra Red Imager (SEVIRI) pixels resolution. The resolution enhancement is obtained by merging data streams from the two instruments (the GERB spatial resolution is about 50 km at nadir, and the SEVIRI resolution is 3 km at the satellite sub-point).

It is worth pointing out that in the absence of reliable GERB data at this time (while Meteosat Second Generation commenced routine operations on 29 January 2004, the GERB instrument is still in validation phase), we will consider in the

following SW fluxes retrieved from Meteosat-7 (MS-7) data using the CERES-TRMM broadband SW ADMs to perform, the SW radiance-to-flux conversion as a surrogate for the GERB SW fluxes at the 3×3 SEVIRI resolution.

This paper is subdivided as follows: first, before describing how the outgoing short wave radiative fluxes are retrieved from MS-7 data, we present the clear oceanic zones and months selected for our sensitivity study. Next, we compare and discuss different ways to provide SW fluxes at the TOA when initial radiance measurements are contaminated by sun glint. Finally, we summarize the conclusions.

2. Study areas definition and selected MS-7 data

Rather than estimating the glint reflectance on every ocean pixel in each MS-7 slot using the illumination and observation geometry of each pixel as well as external knowledge of the wind speed and direction to determine the level of sun glint contribution (Cox and Munk 1954a, b), we have considered here that water pixels located inside a glint angle, γ^1 (see figure 1) threshold value of 15° in each MS-7 slots exhibited a sun glint contamination in the measured visible MS-7 radiance. Note that such a threshold value (which is quite similar to that applied by Giglio *et al.* (2003) on MODIS data) has been chosen to select pixel radiances which are likely to exhibit sun glint (case studies indicate that sun glint may contaminate pixel radiances as far as 40° from the specular angle).

In the following, we have restricted our sensitivity study to the clear oceanic areas defined by a glint angle lower or equal to 15° on the MS-7 07:00, 12:00, and 17:00 UTC time slots during the months of February and July 2003. Similar results are found for other oceanic regions of sun glint occurrence and months. The selected zones are shown in figure 2 for 15 February and 15 July 2003, respectively. As we can see on the panels in figure 2, the glint zone moves westward throughout the day in the MS-7 disk and in latitude during the year. Due to the geostationary orbit of the MS-7 sensor, the sun glint zone can appear with a elliptic shape on the MS-7 disk. By contrast, polar orbiting imageries show an alongated pattern aligned with orbit direction if the satellite subpoint and the solar subpoint are sufficiently close. Finally, for a given day and pre-defined sun glint zone, we have considered all available half-hourly MS-7 slots.

3. Reflected TOA SW flux computation

MS-7, like other imaging radiometers of meteorological satellites, is first designed to make pictures of cloud patterns and accurate radiometric calibrations of their channels are not emphasized. Infrared and water-vapour channel calibration is provided, but there is no onboard calibration system for the visible channel (only a raw estimate of the

---

[1]In a target-fixed, the local coordinates system with the *y*-axis aligned with the sun azimuth, given the sun zenith angle, θ_s, and the sensor zenith angle, θ_v, and the azimuth angle, ϕ, specifying the reflected ray, the specular reflection angle (glint angle), γ, is given by:

$$\cos\gamma = \mu_s\mu_v + \sqrt{(1-\mu_s)^2}\sqrt{(1-\mu_v)^2}\cos\phi$$

where μ_s and μ_v are the cosines of the solar and viewing zenith angles, respectively. Note that on figure 1, α is the scattering angle.
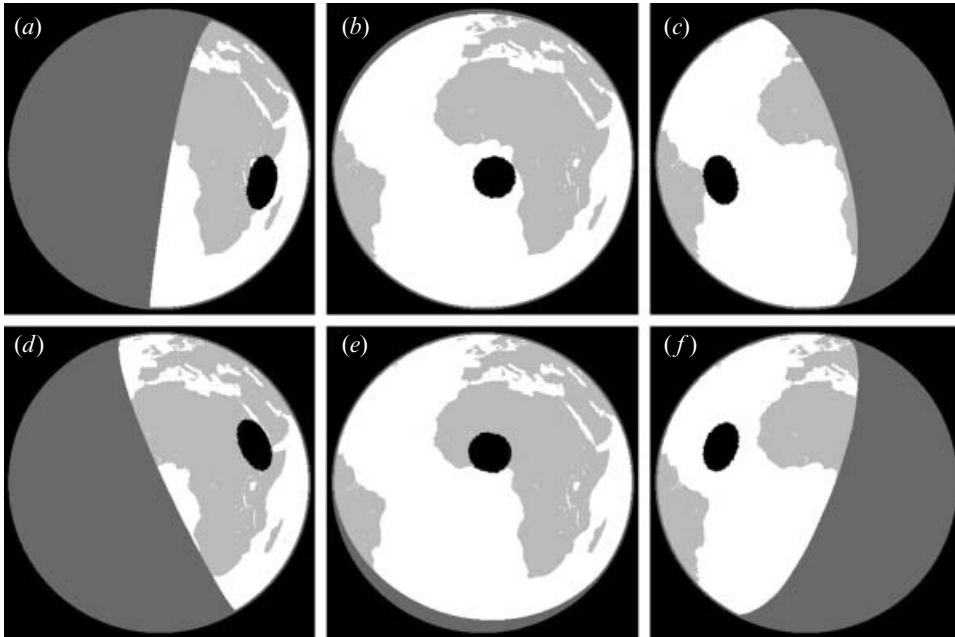
Figure 2. Sun glint area in the MS-7 disk as defined by considering a glint angle threshold value of 15° (black zone in the panels) in the MS-7 (*a*) 07:00, (*b*) 12:00 and, (*c*) 17:00 UTC time slots on 15 February 2003, respectively. The same is provided on 15 July 2003 for the MS-7 (*d*) 07.00, (*e*) 12:00 and, (*f*) 17:00 UTC time slots.

visible channel calibration is provided by Eumetsat). To overcome this weakness, a cross-calibration of the MS-7 visible channel has been performed (Clerbaux 2002) according to the well-calibrated short wave channel of the CERES instrument on the TRMM and Terra low-orbit spacecrafts (Wielicki *et al*. 1996).

MS-7 does not provide the total SW radiance reaching the instrument but only the radiance in its visible channel (0.45–1.0 μm). For this reason, the total SW radiance is estimated from the visible filtered measurements using a third-degree regression on the filtered measurements:

$$L_{sw} = D_0(\theta_s) + D_1(\theta_s)L_{vis} + D_2(\theta_s)L_{vis}^2 + D_3(\theta_s)L_{vis}^3 \tag{3}$$

where the regression coefficients D_i ($i=0, ..., 3$) depend on the solar zenith angle, θ_s, and are obtained by least-mean-square minimization on a database of spectral radiance curves. It is worth pointing out that in equation (3), the narrow band-to-broadband (NB-to-BB) conversion coefficients are neither dependent on the viewing zenith angle nor dependent on the azimuth angle because the radiative transfer model used to generate the spectral radiance database supposes Lambertian surface reflectances.

By contrast to the NB-to-BB SW radiance conversion, our BB radiance-to-flux conversion accounts for the non-isotropic distribution of the radiance. Because most natural surfaces are non-Lambertian, we make use of the newly published CERES-TRMM SW ADMs (Loeb *et al*. 2003) to perform the angular integration. The instantaneous broadband SW flux, F_{ani} is computed from the directional SW broadband radiance by using equation (1) and considering the appropriate CERES ADM scene type.

CERES ADM scene types are defined according to imager-derived cloud (e.g. cloud phase, cloud fraction, and cloud optical depth) and ECMWF meteorological parameters (e.g. wind speed, precipitable water, surface skin temperature, surface emissivity maps, and vertical profiles of temperature and humidity) that have a strong influence on the anisotropy (or angular variation) of the radiance field. Regarding the angular bins resolution, relative azimuth angles range from 0 to 180°, because the models are assumed to be azimuthally symmetric about the principal plane, and ten angular bins are considered for ϕ with a 10 or 20° step. Angular bins for θ_s are defined over the same intervals as for θ_v (nine angular bins from 0 to 90° in 10° steps). This approach is a major advance over the Earth Radiation Budget Experiment (ERBE) (Barkstrom 1984) ADMs, which used coarser resolution. The ERBE SW anisotropic factors (Suttles *et al.* 1988) were calculated as a function of ten solar zenith angles, θ_s, seven viewing zenith angles, θ_v and, eight relative azimuth angles, ϕ.

Finally, because the anisotropy of the Earth's scenes generally varies with viewing geometry and cloud/clear-sky properties in a continuous manner, whereas the CERES ADMs are defined for discrete angular bins and scene, the CERES anisotropic factors have to be adjusted to avoid introducing large instantaneous flux errors or sharp flux discontinuities between angular bins or scene types. To reduce angular bin discretization errors, we estimate anisotropic factors by linearly interpolating bin-averaged anisotropic factors to each observation angle (θ_s, θ_v, ϕ) (in the SW, R, is a function of all three angles). The ADM anisotropic factor, $R_j(\theta_{si}, \theta_{vk}, \phi_l)$, for a given scene type (j), in a given angular bin (θ_{si}, θ_{vk}, ϕ_l) is assumed to correspond to the midpoint of the discrete angular bin defined by ($\theta_{si} \pm \frac{1}{2}\Delta^{\theta_s}$, $\theta_{vk} \pm \frac{1}{2}\Delta^{\theta_s}$, $\phi_l \pm \frac{1}{2}\Delta^{\theta_s}$), where $\Delta\theta_s$, $\Delta\theta_v$, $\Delta\phi$, represent the angular bin resolution, and the estimation of the anisotropic factor for the set of observation angles (θ_s, θ_v, ϕ) is then provided by performing a three-dimensional linear interpolation.

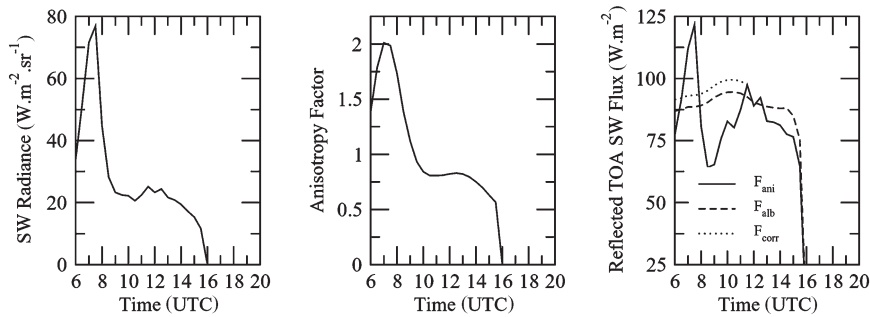## 4. SW fluxes comparison

4.1 F_{ani} *versus* F_{alb}

Figures 3–6 allow comparisons of estimations of the instantaneous reflected clear sky SW fluxes at the TOA as provided by using the standard equation (1) (the F_{ani} solid line on right panels) and the climatological ADM flux estimate equation (2) approach (the F_{alb} dashed line on right panels), respectively, from sun glint containanated SW radiance values (provided on left panels). For both methods, the right-hand-side panels in figures 3–6 provide the time evolution (from sunrise to sunset) of the estimated instantaneous clear sky TOA SW flux over the three pre-defined oceanic regions corresponding to (*a*) the sun glint area computed on the daily MS-7 07:00 UTC time slot, (*b*) the daily MS-7 12:00 UTC time slot, and (*c*) the daily MS-7 17:00 UTC time slot. Note that the appropriate anisotropic factors (displayed on middle panels in each of these figures) as well as the broadband TOA albedo values required by equations (1) and (2), respectively, originate from the clear ocean CERES-TRMM SW ADM 5 (i.e. all wind speeds clear sky ocean ADM).
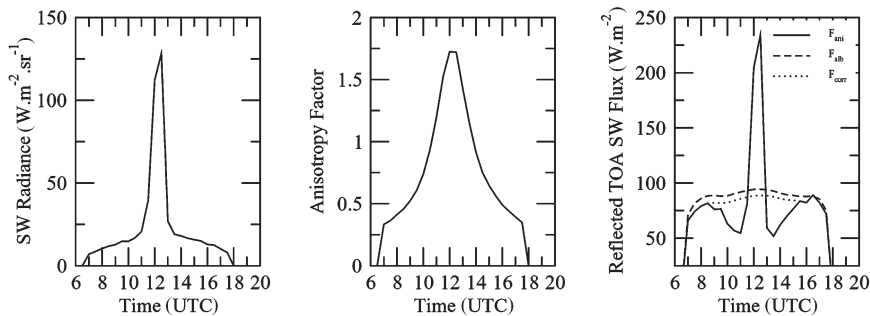
Clearly, whatever the number of clear sky ocean pixels involved in the computation of the displayed SW fluxes time series (figure 3 accounts only for single-pixel time series, figure 4 for areas averaged time series, and finally, figures 5 and 6 for monthly mean and areas averaged time series) and the location of sun glint contamination inside the MS-7 disk, the use of the CERES-TRMM broadband

15 FEBRUARY 2003: SINGLE PIXEL

(*a*) Pre-defined 07h00 UTC Sun Glint Zone

(*b*) Pre-defined 12h00 UTC Sun Glint Zone

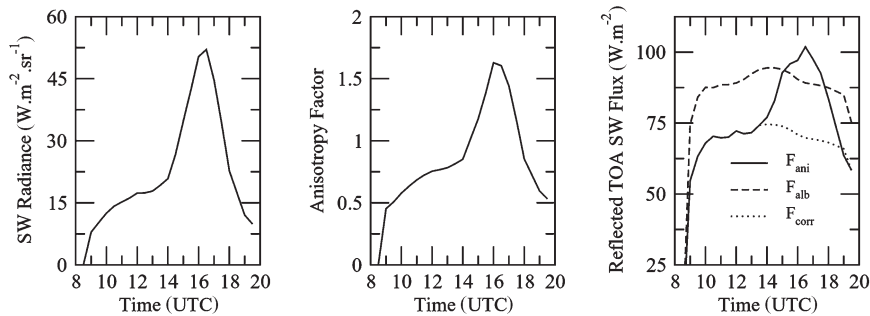### (*c*) Pre-defined 17h00 UTC Sun Glint Zone

Figure 3.   Time evolution (from sunrise to sunset) for a given clear sky oceanic pixel located inside the pre-defined sun glint zone in (*a*) the MS-7 07:00 UTC time slot (figure 2(*a*)), (*b*) the MS-7 12:00 UTC time slot (figure 2(*b*)) and, (*c*) the MS-7 17:00 UTC time slot (figure 2(*c*)) on 15 February 2003 of the SW radiance (left panel), the related clear ocean anisotropic factor from the CERES-TRMM ADM 5 (middle panel), and finally the reflected TOA SW fluxes (right panel). Note that in the right panels, the F_{ani} solid line accounts for SW fluxes computed according to equation (1), the F_{alb} dashed line according to equation (2) and finally the F_{corr} dotted line according to equation (4).

clear ocean SW ADMs anisotropic correction factors does not allow satisfactory retrieval of clear-sky reflected TOA fluxes when SW radiance values are contaminated by sun glint. Related to the ADM anisotropic factor increase during the sun glint perturbation, we observe a large increase in the magnitude of the

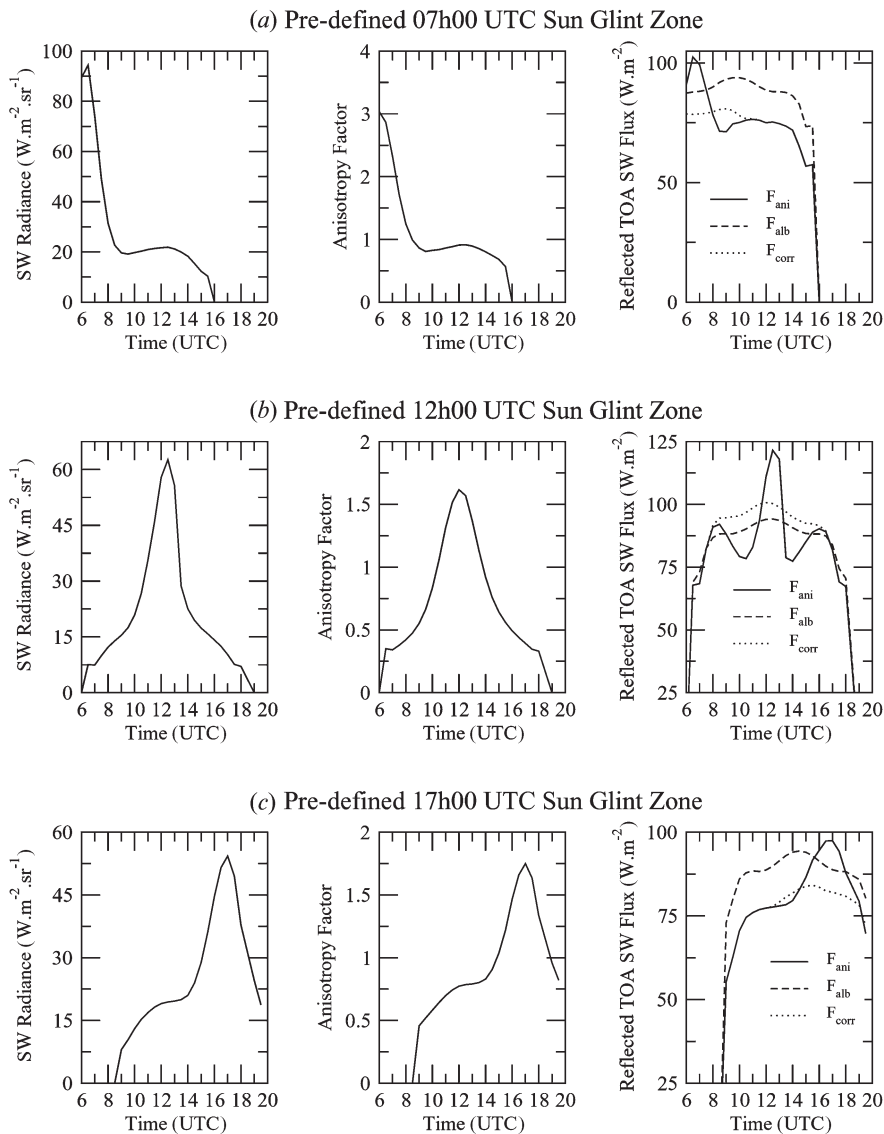## 15 FEBRUARY 2003: DAILY MEAN AND AREA AVERAGED VALUES

(*a*) Pre-defined 07h00 UTC Sun Glint Zone

(*b*) Pre-defined 12h00 UTC Sun Glint Zone

(*c*) Pre-defined 17h00 UTC Sun Glint Zone

Figure 4. Time evolution (from sunrise to sunset) of the area averaged corresponding to (*a*) the MS-7 07:00 UTC time slot (see figure 2(*a*)), (*b*) in the MS-7 12:00 UTC time slot (see figure 2(*b*)) and, (*c*) the MS-7 17:00 UTC time slot (see figure 2(*c*)) pre-defined sun glint zone on 15 February 2003 clear ocean SW radiance (left panel), associated clear ocean anisotropic factor from the CERES-TRMM ADM 5 (middle panel), and finally reflected clear sky TOA SW fluxes (right panel). Note that in the right panels, the F_{ani} solid line accounts for SW fluxes computed according to equation (1), the F_{alb} dashed line according to equation (2) and finally the F_{corr} dotted line according to equation (4).

computed instantaneous fluxes at time of strong sun glint perturbation. As we can see on the right-hand side of figure 3B, the difference between the F_{ani} and F_{alb} fluxes can be as high as 140 W m^{-2} (equivalent to a relative difference between the two fluxes of about 150%) for a given pixel at the time of the strongest sun glint

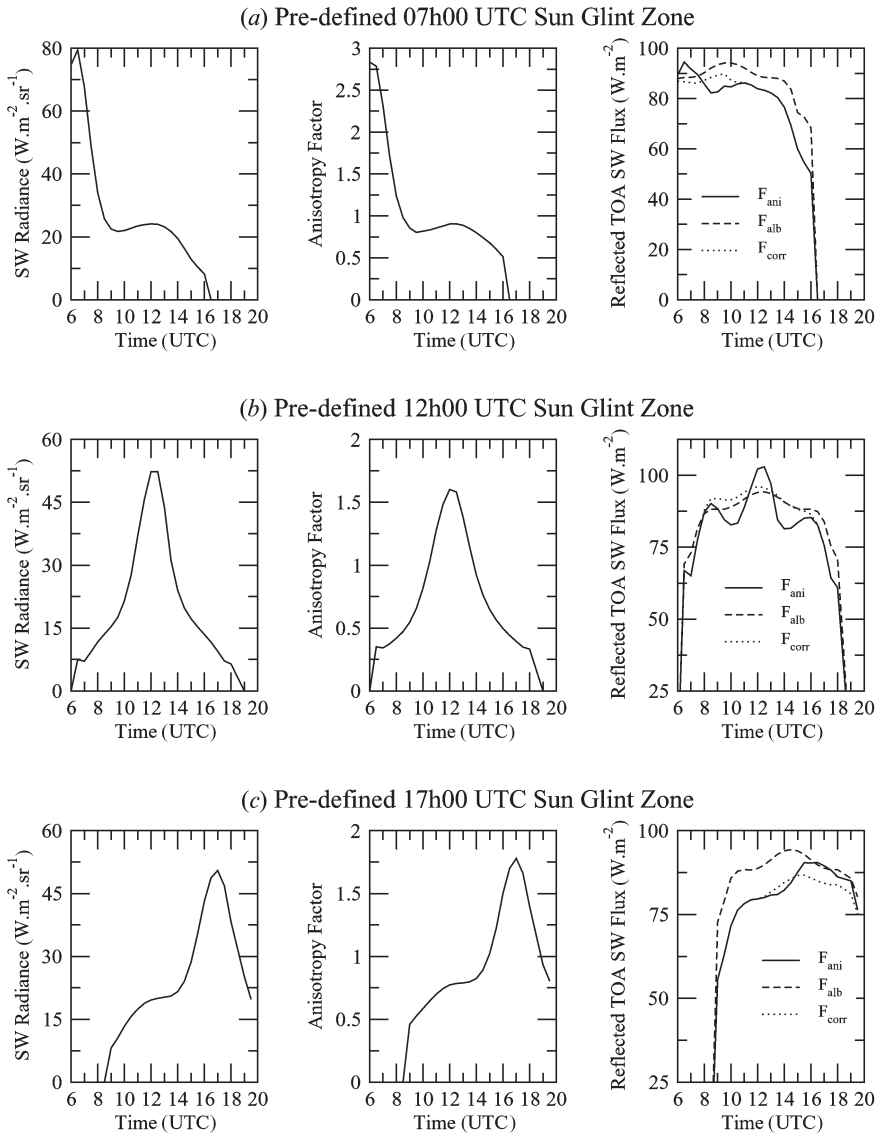FEBRUARY 2003: MONTHLY MEAN AND AREA AVERAGED VALUES

(*a*) Pre-defined 07h00 UTC Sun Glint Zone

(*b*) Pre-defined 12h00 UTC Sun Glint Zone

(*c*) Pre-defined 17h00 UTC Sun Glint Zone

Figure 5. Time evolution (from sunrise to sunset) of the February 2003 monthly mean and pre-defined sun glint zone area averaged computed from (*a*) the daily MS-7 07:00 UTC time slot, (*b*) the daily MS-7 12:00 UTC time slot and, (*c*) the daily MS-7 17:00 UTC time slot clear ocean SW radiance (left panel), associated clear ocean anisotropic factor from the CERES-TRMM ADM 5 (middle panel), and finally reflected clear sky TOA SW fluxes (right panel). Note that in the right panels, the F_{ani} solid line accounts for SW fluxes computed according to equation (1), the F_{alb} dashed line according to equation (2) and finally the F_{corr} dotted line according to equation (4).

contamination. Averaged over all the clear ocean pixels located inside the pre-defined sun glint zone on 15 February 2003, the difference between the two fluxes at time of the strongest sun glint perturbation decreases to about $27\,W\,m^{-2}$ (equivalent to a relative difference of about 28.5%) (see the right-hand side of figure 4(*b*)). This

JULY 2003: MONTHLY MEAN AND AREA AVERAGED VALUES

(*a*) Pre-defined 07h00 UTC Sun Glint Zone

(*b*) Pre-defined 12h00 UTC Sun Glint Zone

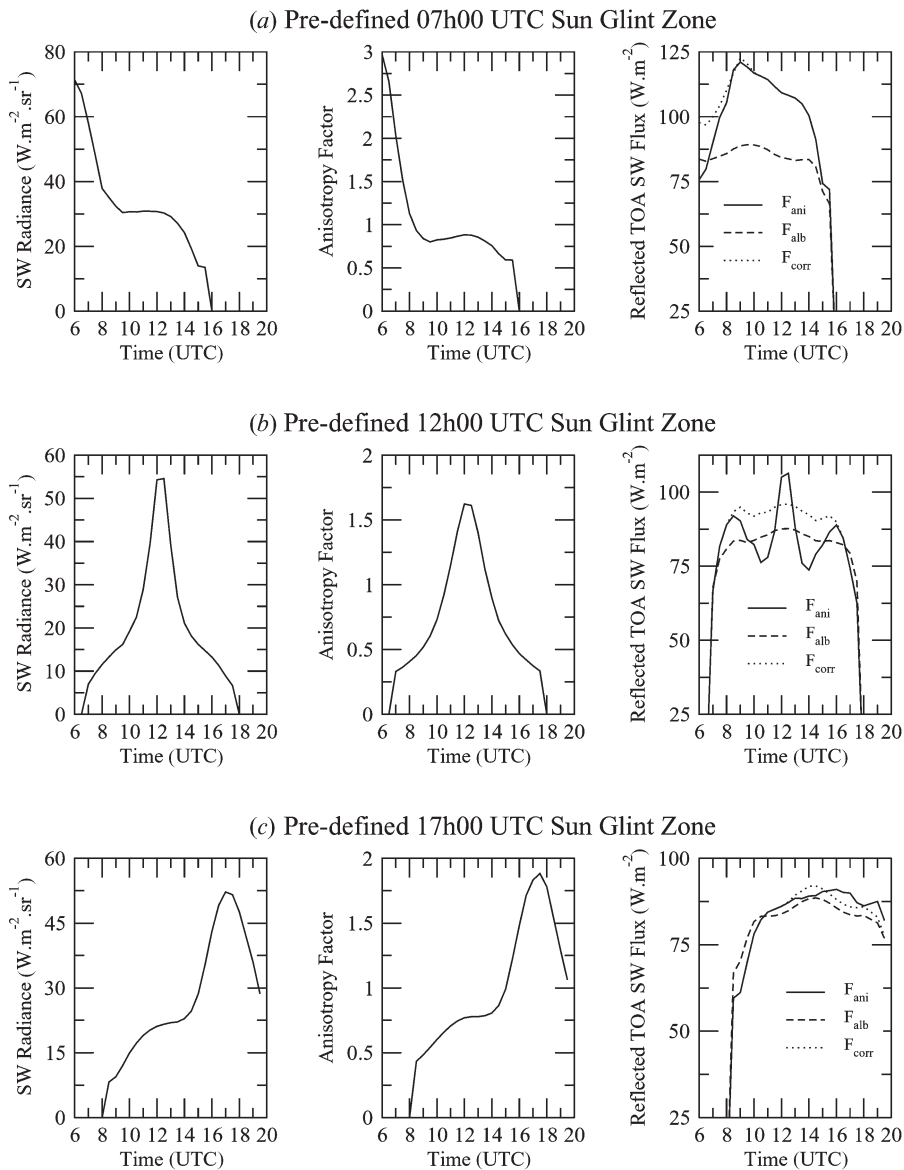#### (*c*) Pre-defined 17h00 UTC Sun Glint Zone

Figure 6.   Time evolution (from sunrise to sunset) of the July 2003 monthly mean and pre-defined sun glint zone area averaged computed from (*a*) the daily MS-7 07:00 UTC time slot, (*b*) the daily MS-7 12:00 UTC time slot and, (*c*) the daily MS-7 17:00 UTC time slot clear ocean SW radiance (left panel), associated clear ocean anisotropic factor from the CERES-TRMM ADM 5 (middle panel), and finally reflected clear sky TOA SW fluxes (right panel). Note that in the right panels, the F_{ani} solid line accounts for SW fluxes computed according to equation (1), the F_{alb} dashed line according to equation (2) and finally the F_{corr} dotted line according to equation (4).

reduction originates in the simple sun glint discrimination method (e.g. a glint angle threshold value) we use to define the sun glint area and the presence of cloudy pixels in the selected area. Indeed, ocean pixels located inside the selected sun glint area are

contaminated differently by sun glint, and the presence of clouds above ocean pixels can potentially unable us to account for strongly contaminated pixels in our clear-sky averaging process. As an example, the right-hand side of figure 5(*b*) reveals that on average for the month of February 2003, the difference between the mean F_{ani} and F_{alb} fluxes for the daily MS-7 12:00 UTC time slot pre-defined sun glint zone is about 7.2 W m^{-2} (equivalent to a relative difference of about 7.5%), while the same in July 2003 accounts for a flux difference of 18 W m^{-2} (equivalent to a relative difference of about 19.5%). This difference between the February and July results originates in the fact that a larger number of strongly contaminated pixels have been included in the clear-sky July averaging process, possibly due to a reduced presence of clouds at times of strong sun glint perturbation in July 2003 compared with February 2003.

Essentially the same is reported regarding the TOA SW F_{ani} and F_{alb} fluxes differences at times of strong sun glint perturbation computed in the daily MS-7 07:00 and 17:00 UTC time slots sun glint areas (see right-hand side of figures 3(*a*)– 6(*a*) and 3(*c*)–6(*c*)), except that the magnitudes of the differences between F_{ani} and F_{alb} are relatively smaller than those reported above for fluxes computed in the daily MS-7 12:00 UTC time-slot sun glint area. Some readers can be dumbfounded by the shape of the F_{ani} flux time series displayed on the right-hand side of figure 6(*a*). Indeed, while the radiance time series provided on the left-hand side of figure 6(*a*) indicates a strong sun glint contamination early in the morning, the related SW flux time series presents a flux magnitude increase from 06:00 to 10:00. This confusing trend results from the simultaneous presence of both ocean pixels and inland water pixels inside the pre-defined daily MS-7 07:00 UTC time-slot sun glint area (see figure 2(*d*)) but in a changing proportion throughout the day. What happens is the progressive increase of the inland water pixels involved in our averaging clear sky process from one MS-7 slot to the other throughout the day. As these inland pixels present a larger surface albedo than ocean pixels, the corresponding enhancement in the reflected SW flux relative to the ocean pixels masks the sun glint perturbation in the flux time series early in the morning.

More surprising is the flux underestimation which is reported prior and after the time of strongest sun glint perturbation when comparing the F_{ani} and F_{alb} time series in the right panels figures 3(*b*)–6(*b*). Based on the difference between the curves F_{ani} and F_{alb} in the right-hand side of figure 3(*b*), we see that the pixel is affected by sun glint from approximately 08:30 to 15:30 (i.e. 7 h). On the other hand, the pixel SW radiance time series (left-hand side of figure 3(*b*)) only reveals a sun glint contamination of about 2 h corresponding to the flux overestimation time period in the F_{ani} time series on the right-hand side of figure 3(*b*). The two time periods of about 2:30 h surrounding the time of strong sun glint perturbation which exhibit a SW flux underestimation originate in CERES-TRMM broadband clear ocean SW ADM anisotropic correction factors (see the middle panel of figure 3(*b*)). ADM anisotropic factors tend to over-correct the SW radiance in the vicinity of the sun glint period when the SW radiance-to-flux conversion is performed. Such an over-correction of the radiance leading to an underestimation of the flux is also found in the F_{ani} time series computed in the daily MS-7 07:00 UTC time slot pre-defined sun glint area (see the right-hand side of figures 3(*a*)–5(*a*)). Although of reduced magnitude, a time period of flux underestimation can also be observed in the F_{ani} time series computed over the daily MS-7 17:00 UTC time slot pre-defined sun glint zone (see the right-hand side of figures 3(*c*)–6(*c*)).

4.2 *Wind speed influence*

As previously mentioned, we have considered until now the CERES-TRMM SW ADM 5 (i.e. all wind speeds clear sky ocean ADM) when performing the radiance to F_{ani} conversion or the F_{alb} interpolation (figures 3–6). However, theoretical calculations have shown that the upward radiance at TOA could behave differently when ocean-surface wind speed and direction change (e.g. Masuda 1998). In contrast to previously derived ADMs (e.g. ERBE ADMs), the effects of ocean winds have been explicitly included in the CERES broadband ADMs. Separate clear ocean SW ADMs have been defined for four intervals of wind speed corresponding to the 0–25th, 25–50th, 50–75th, and 75–100th percentiles of the wind speed probability density function at the 10 m level in addition to an all-wind-speed clear ocean ADM. These correspond to wind-speed intervals of approximately <3.5, 3.5–5.5, 5.5–7.5, and $>7.5 \, \text{m s}^{-1}$.

Figure 7 presents for a given pixel located inside the pre-defined MS-7 12:00 UTC time slot sun glint area on 15 February 2003 the different F_{ani} and F_{alb} flux time series resulting from the conversion of the pixel radiance time series when considering the various wind-speed dependent SW ADMs. As we can see in figure 7(c), the magnitude of the anisotropic factor is inversely proportional to the wind speed. For calm oceans, when the wind speeds are below $3.5 \, \text{m s}^{-1}$, the ocean surface is relatively flat, and the sun light is specularly reflected. The sun glint effects decrease dramatically as the viewing geometries change. At higher wind speeds, the ocean surface acts as diffuse reflectors, and whitecaps are formed (e.g. Cox and Munk 1954a, b). The principal effect of the rough surface is to reflect the direct solar beam into a range of angles; the rougher the sea, the wider the range. Thus, in the sun glint region, sunlight that was supposed to be specularly reflected has been scattered in all directions because the ocean surface no longer reflects like a flat mirror. Therefore, the reflectance in the sun glint region is weakened.

Figure 7(e) indicates that accounting for the wind-speed influence on the ocean's bidirectional reflectance has an impact on the retrieved SW flux value not only at times of strong sun glint perturbation but also during the time period surrounding the sun glint perturbation. First, while the magnitude of the reflected solar radiation is inversely proportional to the wind speed, none of the five clear ocean wind-speed-dependent ADMs copes satisfactorily with the sun glint contamination of the SW radiance given in figure 7(a). Whatever the wind speed range may be, all the five computed F_{ani} flux time series overestimate the magnitude of the reflected TOA SW flux at time of strong sun glint perturbation in comparison with the magnitude range reported when interpolating the clear ocean wind-speed-dependent ADM flux at the solar zenith angle of observations (see figure 7(f)). Second, the magnitude of the flux underestimation which occurs in the region surrounding the strong sun glint perturbation is inversely proportional to the wind speed. Third, figure 7(e) shows that the retrieved fluxes exhibit some ADMs dependent fluctuations, as these fluctuations cannot be explained by the shape of the SW radiance given in figure 7(a). This is particularly well illustrated in figure 7(e) for the time period ranging from 9:00 to 12:00. By contrast, fluctuations reported from 15:00 to 17:00 in figure 7(e) can be detected in the SW radiance time series in figure 7(a).

These deficiencies in the SW fluxes estimation could originate in the CERES ADMs angular bins resolution. Anisotropy of Earth's scenes generally varies with viewing geometry (and cloud/clear-sky properties) in a continuous manner, whereas the CERES ADMs are defined for discrete angular bins (and scene types). To overcome such a difficulty, we estimate anisotropic factors by linearly interpolating
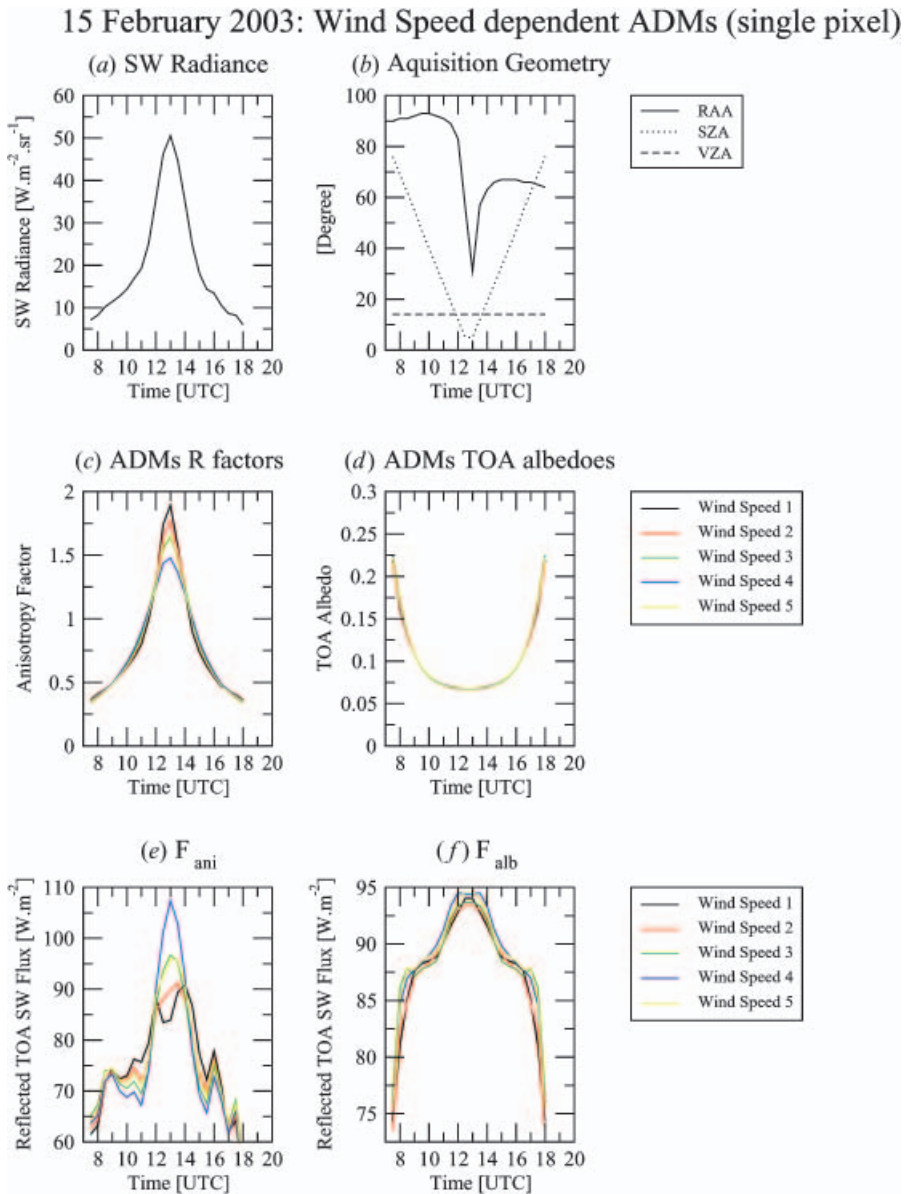
15 February 2003: Wind Speed dependent ADMs (single pixel)

Figure 7. Wind-speed influence on the bidirectional reflectance of the ocean. The evolution (from sunrise to sunset on 15 February 2003) of (*a*) the clear-sky SW radiance for a given pixel located inside the MS-7 12:00 UTC time slot pre-defined sun glint area with acquisition geometry throughout the day provided panel (*b*) (RAA=relative azimuth angle, SZA=solar zenith angle and, VZA=viewing zenith angle). The corresponding CERES-TRMM SW ADM anisotropic factor and TOA broadband albedo are displayed panels (*c*) and (*d*), respectively. Panel (*e*) presents the reflected TOA SW fluxes time series resulting from the radiance-to-flux conversion. Finally, panel (*f*) displays the wind-speed-dependent clear-sky ADMs fluxes interpolated at each pixel solar zenith angle of observation.

bin-averaged ADM anisotropic factors to each observation angle. However, a bias in the retrieved flux will occur if linear interpolation is performed when the actual radiance varies nonlinearly within an angular bin. This is unfortunately the case when measured radiances are contaminated by sun glint.

5. Temporal interpolation of fluxes from existing ADMs

As we can see, a number of limitations occur when computing instantaneous TOA SW flux from a radiance measurement contaminated by sun glint. When sun glint is observed by CERES (which flies on sun synchronous or precessing orbits), the CERES algorithm avoids making a radiance-to-flux retrieval. Instead, it uses climatological TOA albedos determined empirically for the wind speed and solar zenith angle corresponding to the observation (Loeb *et al.* 2003) (i.e. the F_{alb} solution in equation (2)). A limitation with such climatological SW fluxes (CERES-TRMM SW broadband ADMs only provide annual mean values and do not account for seasonal changes) relies on their climatological magnitude, which can be quite different from the actual SW flux magnitude on a given day or month in the year. Such a magnitude difference is apparent in the right-hand side panels of figures 3–6 when comparing the F_{ani} and F_{alb} SW fluxes time series outside the temporal region(s) affected by sun glint. As an example, the right-hand side figure 3(c) indicates that the difference between the retrieved and the climatological SW flux prior to the sun glint contamination can be as high as $20 \, W \, m^{-2}$ (equivalent to a relative difference of about 25%) for a given pixel located inside the pre-defined MS-7 17:00 UTC time slot sun glint area on the 15 February 2003. Averaged over the daily MS-7 17:00 UTC time slot sun glint area, the right-hand side of figure 5(c) reveals that the monthly mean difference between the two fluxes time series still reaches as high as about $14 \, W \, m^{-2}$ (equivalent to a relative difference of about 17%) outside the sun glint region for February 2003. On the other hand, the difference between the two fluxes time series reduces to a few $W \, m^{-2}$ for July 2003 (see right-hand side of figure 6(c)). Therefore, according to the location and the time in the year, figures 3–6 reveal that while masking the imperfections resulting from the radiance-to-flux conversion, a shift from the F_{ani} time series to the F_{alb} time series at the time of sun glint perturbation could artificially increase or decrease the magnitude of the reflected TOA SW flux.

  To overcome such difficulties, we suggest that advantage should be taken of both the high temporal sampling of the sun glint region afforded by the geostationary orbit of the Meteosat satellites and the information contained in the empirical clear ocean CERES-TRMM broadband SW ADMs. Namely, the method simply involves multiplying the clear ocean wind-speed-dependent ADM flux interpolated at the solar zenith angle of observation (Loeb *et al.*'s (2003) F_{alb} solution) by a correction factor, $X(t)$, allowing to account for the actual radiance measurements. The estimated flux in sun glint (F_{corr}) at time t, is determined using the following expression:

$$F_{corr}(t) = F_{alb}(t).X(t) \tag{4}$$

where, $F_{alb}(t)$ is the climatological ADM flux estimate and $X(t)$ a correction factor allowing to account for actual radiance measurements:

$$X(t) = \frac{F_{ani}(t_i)}{F_{alb}(t_i)} + \frac{\dfrac{F_{ani}(t_f)}{F_{alb}(t_f)} - \dfrac{F_{ani}(t_i)}{F_{alb}(t_i)}}{t_f - t_i}.(t - t_i) \tag{5}$$

where t_i and t_f define the time interval during which the correction is applied. By setting t_i equal to the time of the first local maximum appearing (due to the fluxes underestimation occurring when using the CERES ADMs anisotropic factor in regions surrounding the sun glint contamination to retrieve the reflected solar flux) in the F_{ani} clear sky, TOA reflected SW flux time series, and t_f to the third local maximum (the second local maximum being due to the flux overestimation at time of strong sun glint perturbation), we are able to correct both underestimated as well as overestimated fluxes. As we can see, during sun glint, the method does not actually provide a radiance-to-flux conversion but rather interpolates fluxes made prior and after sun glint. Note that for sun glint contamination of radiance measurements occurring in the vicinity of the sunrise (sunset), the correction factor, $X(t)$, is taken as invariant in time because only the left (right) part of the underestimation–overestimation–underestimation cycle is available from the F_{ani} time series and it will correspond to the ratio of $F_{ani}(t_f)/F_{alb}(t_f)$ $(F_{ani}(t_i)/F_{alb}(t_i))$. Similarly, for a cloud-contaminated radiance measurement at time t_i (t_f), clear sky flux $F_{ani}(t_i)$ $(F_{ani}(t_f))$ cannot be estimated, and the correction factor, $X(t)$, will be given by the ratio $F_{ani}(t_f)/F_{alb}(t_f)$ $(F_{ani}(t_i)/F_{alb}(t_i))$. Finally, when both $F_{ani}(t_i)$ and $F_{ani}(t_f)$ are undetermined due to cloud contaminations of the radiance measurements, the correction factor, $X(t)$, is set to 1.

The F_{corr} dotted lines on the right-hand side of figures 3–6 illustrates the effect of our correction factor on the retrieved instantaneous SW fluxes at the TOA. The benefit of the correction factor over a simple interpolation of the ADM flux at the solar zenith angle of observations is apparent if we compare, for example, the F_{corr} curve (dotted line) with the F_{alb} curve (dashed line) on the right-hand side of figure 3.

6.   Final discussion and conclusions

Because satellite radiometers do not measure the instantaneous reflected SW flux at the TOA directly, ADMs are required to relate the actual radiance measurement to flux at a given solar angle, satellite-viewing geometries, and surface and atmospheric conditions. Considering the newly developed CERES-TRMM broadband SW ADMs (Loeb *et al.* 2003), we have investigated if the associated anisotropic correction factors allow clear-sky reflected SW TOA fluxes to be satisfactorily retrieved when radiance measurements are contaminated by sun glint. Analyses of TOA outgoing SW radiative flux time series estimated from MS-7 visible radiance measurements over pre-defined oceanic areas of sun glint occurrence have highlighted some limitations when performing radiance-to-flux retrievals in sun glint that are directly related to the ADMs.

First, while CERES-TRMM SW ADMs present a major advance over ERBE ADMs, the angular bins used to define CERES ADMs are unfortunately still too coarse to adequately account for the large radiance variations when satellite viewing geometry moves towards the ocean specular reflection zone. Namely, our results indicate that using the anisotropic correction factors from the clear ocean CERES-TRMM broadband SW ADMs to retrieve the outgoing clear-sky SW flux at the TOA leads to an overestimation of the flux magnitude in the sun glint region and, on the contrary, an underestimation in the surrounding regions.

Second, while an estimation of anisotropic factors by linearly interpolating CERES-TRMM SW ADMs bin-averaged anisotropic factors to each observation angle can reduce angular bin discretization errors, such an interpolation can bias the

SW flux computation when radiance measurement is contaminated by sun glint because the actual radiance varies nonlinearly within the angular bin.

Taking advantage of the high temporal sampling afforded by the geostationary orbit of the Meteosat-7 satellite and the information enclosed in the CERES-TRMM broadband SW ADMs, we have shown that it is possible to provide valuable, better clear-sky SW flux estimation from radiance measurements contaminated by sun glint. By interpolating the clear ocean wind-speed-dependent ADM TOA albedo at the solar zenith angle of observations, Loeb *et al.* (2003) were only able to compute and deliver instantaneous ADM climatological fluxes values. Here, by taking into account all visible MS-7 slots over a day, we are able to identify for each pixel, which had radiance measurements affected by sun glint, the full underestimation–overestimation–underestimation cycle in the retrieved instantaneous SW fluxes time series. This allows us to substitute all the erroneous fluxes in the time series by the clear ocean wind-speed-dependent ADM fluxes interpolated at the solar zenith angle of observations as in Loeb *et al.* (2003) but scaled in order to account for actual radiance measurements. Information from instantaneous clear-sky SW fluxes retrieved before and after the sun glint contamination of the measured radiances is used to determine the magnitude of the scaling factor.

However, as our scheme does not actually provide a radiance-to-flux conversion during sun glint, but rather interpolates fluxes made prior and after sun glint, if wind speed or aerosol conditions suddenly change during sun glint and return to their initial conditions after sun glint, the change would not be observed in the TOA flux time series. This certainly constitutes a severe limitation in the accuracy of the delivered geostationary SW flux, as we have seen that for a water pixel sampled by a geostationary radiometer, the signature of the sun glint contamination in its SW flux time series can reach up to 7 h over the day. Therefore, the accuracy of the estimated SW fluxes should ideally be inferred each time at least one other instrument looks simultaneously at the same ocean target but from different angles allowing a glint-free scene.

References

BARKSTROM, B.R., 1984, The Earth Radiation Budget Experiment (ERBE). *Bulletin of the American Meteorological Society*, **65**, pp. 1170–1186.

CLERBAUX, N., 2002, *Meteosat Count Versus CERES-TRMM Unfiltered Radiance*, RMIB GERB Technical Note MSG-RMIB-GE-TN-0036, Brussels.

COX, C. and MUNK, W., 1954a, Measurements of the roughness of the sea surface from photographs of the sun's glitter. *Journal of the Optical Society of America*, **44**, pp. 838–850.

COX, C. and MUNK, W., 1954b, Statistics of the sea surface derived from sun glitter. *Journal of Marine Research*, **13**, pp. 198–227.

GIGLIO, L., DESCLOITRES, J., JUSTICE, C.O. and KAUFMAN, Y.J., 2003, An enhanced contextual fire detection algorithm for MODIS. *Remote Sensing of the Environment*, **87**, pp. 273–282.

HARRIES, J.E. and CROMMELYNCK, D., 1999, The geostationary earth radiation budget experiment on MSG-1 and its potential applications. *Advances in Space Research*, **24**, pp. 915–919.

KUMMEROW, C., BARNES, W., KOZU, T., SHIUE, J. and SIMPSON, J., 1998, The Tropical Rainfall Measuring Mission (TRMM) sensor package. *Journal of Atmospheric and Oceanic Technology*, **15**, pp. 809–817.

LOEB, N.G., KATO, S. and WIELICKI, B.A., 2002, Defining top-of-atmosphere flux reference level for Earth radiation budget studies. *Journal of Climate*, **15**, pp. 3301–3309.

LOEB, N.G., SMITH, N.M., KATO, S., MILLER, W.F., GUPTA, S.K., MINNIS, P. and WIELICKI, B.A., 2003, Angular distribution models for top-of-atmosphere radiative flux estimation from the clouds and the Earth's radiative flux estimation from the clouds and the Earth's radiant energy System Instrument on the Tropical Rainfall Measuring Mission Satellite. Part I: Methodology. *Journal of Applied Meteorology*, **42**, pp. 240–265.

MASUDA, K., 1998, Effects of the speed and direction of surface winds on the radiation in the atmosphere–ocean system. *Remote Sensing of Environment*, **64**, pp. 53–63.

RAMANATHAN, V., 1987, The role of Earth radiation budget studies in climate and general circulation research. *Journal of Geophysical Research*, **92**, pp. 4075–4095.

SCHMETZ, J.P., PILI, S., TJEMKES, D., JUST, J., KERKMANN, S., ROTA, and RATIER, A., 2002, An introduction to Meteosat second Generation (MSG). *Bulletin of the American Meteorological Society*, **83**, pp. 977–992.

SMITH, G.L., GREEN, R.N., RASCHKE, E., AVIS, L.M., SUTTLES, J.T., WIELICKI, B.A. and DAVIES, R., 1986, Inversion methods for satellite Studies of the Earth's radiation budget: Development of algorithms for the ERBE mission. *Reviews of Geophysics*, **24**(2), pp. 407–421.

SUTTLES, J.T., GREEN, R.N., MINNIS, P., SMITH, G.L., STAYLOR, W.F., WIELICKI, B.A., WALKER, I.J., YOUNG, D.E., TAYLOR, V.R. and STOWE, L.L., 1988, *Angular Radiation Models for Earth–Atmosphere Systems, Vol. I—Short Wave Radiation*, Repory NASA RP-1184, NASA, Washington, DC.

WIELICKI, B.A., BARKSTROM, B.R., HARRISON, E.F., LEE III R.B., SMITH, G.L. and COOPER, J.E., 1996, Clouds and the Earth's Radiant Energy System (CERES): An Earth observing system experiment. *Bulletin of the American Meteorological Society*, **77**, pp. 853–868.